Tunable optical and plasmonic response of Au nanoparticles embedded in Ta-doped TiO_2 transparent conducting films

Cristina Mancarella [1,*] Maria Sygletou [2] Beatrice R. Bricchi [1] Francesco Bisio [3] and Andrea Li Bassi [1,4,†]

[1] *Micro- and Nanostructured Materials Laboratory, Dipartimento di Energia, Politecnico di Milano, via Ponzio 34/3, 20133 Milano, Italy*

[2] *OptMatLab, Dipartimento di Fisica, Università di Genova, I-16146, Genova, Italy*

[3] *SuPerconducting and other INnovative materials and devices institute (SPIN), Consiglio Nazionale delle Ricerche (CNR), Corso F.M. Perrone 24, 16152 Genova, Italy*

[4] *Center for Nanoscience and Technology (CNST), Istituto Italiano di Tecnologia (IIT), via Pascoli 70/3, 20133 Milano, Italy*

(Received 10 September 2021; accepted 24 January 2022; published 11 February 2022)

Localized surface plasmon resonances (LSPRs) are fascinating optical phenomena occurring in metal nanostructures, like gold nanoparticles (NPs). Plasmonic excitation can be tailored efficiently in the visible range by acting on size, shape, and NP surroundings, whereas carrier density is fixed, thus restricting the LSPR modulation. Transparent conductive oxides (TCOs), on the other hand, are gaining increasing interest for their transparency, charge carrier tunability, and plasmonic features in the infrared. The combination of these two materials into a metal-TCO nanocomposite can give access to unique electrical and optical characteristics, to be tailored in view of the desired optoelectronic application. In this paper, Au NPs and Ta-doped TiO_2 TCO films have been merged with the aim to master the Au plasmon resonance by acting on the dielectric properties of the surrounding TCO. Morphology, structure, and electrical properties have been investigated as well to understand the optical response of the nanosystems. The role of the embedding geometry has been explored, revealing that the largest LSPR shift (550–760 nm) occurs when the NPs are sandwiched in the middle of the film and not at the bottom of the film (substrate-film interface). Ta doping in the TCO has been varied (5–10% at. and bare TiO_2) to induce a permittivity change of the matrix. As a result, Au LSPR is clearly blueshifted when decreasing the dielectric permittivity at higher Ta content in the sandwich configuration. Despite the nonoptimal electrical performance caused by defectivity of the films, Au-Ta:TiO_2 multifunctional nanocomposites are promising candidates for their optical behavior as highly tunable plasmonic conductive metamaterials for advanced light management.

DOI: 10.1103/PhysRevMaterials.6.025201

I. INTRODUCTION

Noble metal (Au, Ag) nanoparticles (NPs) have been the subject of intensive research efforts deriving from the possibility to sustain localized surface plasmon resonances (LSPRs) [1,2], known as light-driven collective oscillations of electrons at metal-dielectric interfaces or when confined down to nanometric sizes [3]. LSPR effects have been extensively designed to maximize light-matter interaction in specific spectral ranges by acting on nanostructure parameters. Some of them are NP size, shape [4,5], or interparticle distance [6,7], as well as the metal composition [8,9]. Gold is fairly appointed as the most employed plasmonic material for its outstanding chemical inertness, biocompatibility, and high-quality LSPR excitation in the visible range [10]. The plasmon resonance is highly sensitive to the dielectric properties of the surroundings [11,12], a capability that makes noble metal NPs eligible for several plasmon-enhanced technologies spanning photovoltaics [13,14], photocatalysis [15,16], and sensing [17,18]. However, their applicability in efficient and tunable plasmonic systems was found to be challenging. Indeed, playing with NP geometry is not sufficient for a fine tailoring of the LSPR nature in a wider frequency region, as the major constraint for metals is imposed by the nonmodifiable charge carrier density ($\sim 10^{22}$ cm^{-3}) [19], i.e., the fixed plasma frequency [20].

Recently, attention has been directed toward metal-semiconductor nanocomposites. Indeed, by exploiting the dependence of the plasmon resonance from the surrounding material, the introduction of metal NPs in oxide semiconductors could open the opportunity to indirectly control their plasmonic response. This approach paves the way toward complex systems with an inherent multifunctional nature, enabling unique properties to be reached, strongly influenced by the metal-host pair as demonstrated by plenty of examples in many research fields. Indeed, architectures based on plasmonic-functionalized semiconductors (Au-ZnO, Ag-CeO_2, Au-TiO_2) have been studied in detail for the tunable charge carrier dynamics at the metal-semiconductor interface in photocatalysis [21–24]. Other combined systems, such as Au-ZnO, take advantage of the antimicrobial properties of ZnO and plasmonic excitations typical of Au NPs for the development of optical sensing devices for fast molecule detection [25]. Regarding bioscience, the broadband LSPR absorption driven by coalesced NPs is exploited in Au-Al_2O_3

*cristina.mancarella@polimi.it
†andrea.libassi@polimi.it

and Au/Ag-TiO_2 substrates for surface enhanced Raman spectroscopy [25–27]. Most of the previous studies have examined the influence of the quantity of metal and annealing temperature on NP morphology and structure.

The next step in next-generation plasmonic nanocomposites involves the replacement of the oxide matrix with a transparent conductive oxide (TCO). Being a subclass of doped semiconductors, TCOs have wide bandgaps (>3 eV) and degenerate carrier densities ($>10^{20}\,cm^{-3}$), thus combining high visible transparency (>80%) and low resistivity ($10^{-3}\,\Omega\,cm$ or less) [28,29]. Additionally, charge carrier concentration can be easily manipulated by means of *n*- or *p*-type doping [28] inducing changes on the optical constants of the material [30,31]. This characteristic is crucial when dealing with nanocomposite design since plasmonic control can be reached directly by tuning the carrier density of the matrix. The most studied TCOs are Sn-doped In_2O_3 (ITO), Al-doped ZnO (AZO), and F-doped SnO_2 (FTO) [19], whose features are widely employed in electrodes in solar cells [32–34] and many other applications [35–37]. More recently, doped TiO_2 has been developed as an *n*-type TCO, such as Nb- or Ta-doped TiO_2 [38–41]. Ta:TiO_2 can outperform the more studied Nb:TiO_2 for its enhanced dopant solubility, lower effective mass, and higher mobility [42]. Furthermore, carrier density can be additionally varied by playing with oxygen stoichiometry, which is known to affect defect chemistry and carrier density [43].

Despite the great potential given by joining metal and TCO properties, few works deal with the subject, focusing mainly on high-quality TCOs for light-driven applications [44–49] and biosensors [50]. Huang *et al.* [51,52] reported the possibility to increase carrier concentration, without affecting mobility, exploiting Ag NPs added in AZO films, with the aim to improve electrical conductivity by engineering an ohmic contact at the interfaces where electrons can freely flow. Other studies demonstrated the improvement of electrical performance in TCOs by providing a continuous metal mesh for enhanced conduction [48]. Notably, Ag-AZO and Au-ITO systems have been developed to exploit the amplified light scattering of plasmonic NPs for enhancement of solar cell efficiency [53]. However, the employment of the doping content of a TCO matrix to further tailor the LSPR of embedded NPs is scarcely reported in literature. The carrier-concentration control easily obtainable in doped semiconductors is a powerful tool to engineer the dielectric function without changing the material. TiO_2-based TCOs, particularly Ta:TiO_2, can exhibit variable optical and electrical features, by controlling the Ta amount and oxygen stoichiometry during the deposition [43] or annealing process [38,43]. An additional degree of tuning is attributed to the configuration of the NPs, sensitive to different electrical permittivity according to the position in the film [50].

In this paper, multifunctional metal-TCO nanocomposites were fabricated by embedding Au NPs (approximately with diameter of 25 nm) in Ta-doped TiO_2 films obtained through thermal evaporation of Au, pulsed laser deposition (PLD) of Ta:TiO_2, and multiple ad hoc thermal treatments. PLD was selected for the well-known capability of mastering the TCO morphology and composition by operating directly on synthesis parameters [43]; at the same time, thermal evaporation was used as a method for Au NPs being quick, low cost, and easy to handle.

In this paper, we aim at tailoring experimentally the LSPR of Au NPs by appropriately changing the dielectric matrix using two approaches. First, the role of the NP integration geometry has been analyzed by incorporating Au NPs at different locations. Two systems have been considered: Au NPs fully embedded in TCO film in a *sandwich like* configuration and Au NPs at the interface between TCO and glass substrate, denoted as *bottom* configuration. The second approach consists of varying the Ta doping level in the TCO (5–10% at. and bare TiO_2) to exploit a permittivity change of the matrix. In view of a possible application in optoelectronics, extensive optical analyses were performed in parallel with a full material characterization in terms of morphology, electrical, and structural properties.

II. EXPERIMENTAL METHODS

A. Sample preparation

PLD was performed in a vacuum chamber, equipped with a primary and turbomolecular pumping system, gas inlets, and mass flow controllers to monitor the partial pressure of gaseous species during the deposition process. The laser source was a nanosecond-pulsed Nd:YAG laser (second harmonic, $\lambda = 532\,nm$ green, repetition rate 10 Hz, and pulse duration 5–7 ns). The pulsed laser beam was focused on the target material with an angle of 45 ° with respect to the normal direction of the target surface, subjected to rototranslation to ensure a uniform ablation. All Au-TCO composites were deposited over Si (100) and soda-lime glass substrates, mounted on a rotating sample holder with fixed target-to-substrate distance (50 mm). Glass substrates were cleaned in an ultrasonic bath with isopropanol before deposition.

Ta:TiO_2 thin films with 5 and 10% at. of Ta [also referred as TCO Ta 5% and TCO Ta 10% or Ta(5%):TiO_2 and Ta(10%):TiO_2] were fabricated by ablating Ta_2O_5:TiO_2 targets (99.99% purity) with molar ratio 0.025:0.975 and 0.05:0.95, respectively, all provided by Testbourne Ltd. To synthetize TiO_2 thin films, a TiO_2 target was employed (99.99% purity, provider Kurt J. Lesker). The laser fluence on the targets was set to $2.27\,J\,cm^{-2}$ for TiO_2 and Ta(5%):TiO_2, and $2.73\,J\,cm^{-2}$ for Ta(10%):TiO_2. The fluence was increased by keeping the pulse energy fixed at 150 mJ while varying the spot area onto the target from 6.6 to $5.5\,mm^2$. Ta:TiO_2 films with 10% at. of Ta required a higher fluence to avoid delamination and maximize compactness and crystallinity. All samples were deposited at room temperature and in a background O_2 pressure of 1 Pa. As-deposited TiO_2-based thin films are amorphous; thus, annealing treatments are necessary to achieve crystallization in single-phase polycrystalline anatase. Pure TiO_2 composites were treated in air at 500 °C, 2 h dwell, 4 °C/min ramp to get a fully dielectric matrix. On the other hand, Ta:TiO_2 systems require annealing in a reducing atmosphere (e.g., vacuum) to maintain the oxygen-poor condition contributing to conduction [43]. The latter was performed in a homemade furnace (base pressure 5×10^{-5} Pa) at 550 °C, 1 h dwell at 10 °C/min ramp. Au NPs were produced by thermally evaporating Au grains (99.99% purity) in a gold

layer using an Edwards E360 thermal evaporator, followed by ad hoc thermal treatments to induce thermal solid-state dewetting into NPs with an average horizontal diameter of 20–25 nm, unchanged for all the configurations. Such dimensions were obtained by depositing a gold layer with equivalent thickness of 3 nm, measured by means of a quartz crystal microbalance.

All Au NPs in Au-bottom configurations were formed on Si (100) and soda-lime glass, after annealing in air at 500 °C, 2 h dwell (4 °C/min ramp) in a Lenton muffle furnace; Au-bottom samples were then fabricated by capping Au NPs with TiO_2 or Ta:TiO_2 films, followed by a final annealing step to crystallize the film with thickness of 70 nm. In the case of Au-sandwich samples, the method of preparation required multiple steps of film deposition and annealing to both crystallize the matrix and favor gold dewetting. The first step involved the deposition of 35-nm-thick TiO_2-based film, followed by Au evaporation in the second step; in the third step, TCO/Au was subjected to annealing to get TCOs/Au NPs and crystallize the TCO film. Finally, another TCO layer was deposited with a subsequent annealing to allow its crystallization (fourth step). All the nanocomposites have a total thickness of 70 nm. Figure S1 in the Supplemental Material [54] summarizes with a schematic representation the synthesis steps required for producing Au-TCO nanocomposites.

B. Sample characterization

The morphology of Au-TCO systems was characterized by field emission scanning electron microscopy (FEG-SEM, Zeiss SUPRA 40) for samples deposited on silicon. All geometrical parameters of Au NPs (average diameter, coverage) were extracted with statistical analyses using IMAGEJ software. Additional surface characteristics, particularly NP height, were investigated on selected samples (see Supplemental Material [54]) with atomic force microscopy (AFM, Thermomicroscope Autoprobe CP Research) imaging in tapping mode using VEECO-RTESPA tips with 8 nm curvature radius.

The structure of TiO_2-based films was characterized via Raman spectroscopy (Renishaw InVia micro-Raman spectrometer); the Raman spectra were collected with excitation by an argon ion laser ($\lambda = 514$ nm, green) with the laser power reaching the sample fixed at 0.13 mW to minimize the probability of sample damage by the laser.

Electrical properties and Hall effect measurements were carried out in the four-point probe configuration with a Keithley K2400 Source/Measure Unit as a current generator (from 100 nA to 10 mA), an Agilent 34970A voltage meter, and a 0.57 T Ecopia permanent magnet.

Optical transmittance (T) and reflectance (R) spectra (range $250 - 2000$ nm) were evaluated with a UV-vis-NIR PerkinElmer Lambda 1050 spectrophotometer with a 150 mm diameter integrating sphere. This setup enables the measurement of total T and R, meaning that light transmitted or reflected by the film is collected at all angles. Then logarithmic absorbance of thin film nanocomposites (refer to Supplemental Material [54]) was obtained by performing $-\ln[T/(100-R)]$. Direct transmittance measurements (T component collected with the same direction as the incident one) were recorded in the visible range (190–1100 nm) on selected samples by means of a UV-1800 UV-VIS Shimadzu spectrophotometer. All acquired spectra were normalized with respect to the glass substrate contribution.

Spectroscopic ellipsometry was performed by means of a J.A. Woollam V-VASE ellipsometer (0.5–5.05 eV range, incidence angle of 60 °) on selected samples on silicon substrates: (i) TiO_2 annealed in air at 500 °C for 2 h, 195 nm thick, (ii) Ta(5%):TiO_2 annealed in vacuum at 550 °C for 1 h, 92 nm thick, and (iii) Ta(10%):TiO_2 annealed in vacuum at 550 °C for 1 h, 184 nm thick. For the effective modeling of the optical properties of the Au-NP layer parametric semiconductor (PSEMI) oscillators were applied [55,56], known to be widely employed for modeling the optical response of crystalline materials.

III. RESULTS AND DISCUSSION

A. Morphology and structure

Thermally evaporated Au NPs have been integrated in bare TiO_2 and Ta-doped TiO_2 (5,10% at.) films (70 nm thick), deposited through PLD. Optimization studies, based on previous works [43,57], led to the selection of 1 Pa of O_2 pressure during TCO synthesis, along with postdeposition thermal treatments in a reducing environment (vacuum). These conditions are required to obtain high conducting and crystalline TiO_2-based TCOs (in anatase phase) [57], as discussed in the Experimental Methods.

Before embedding, Au NPs were created from evaporated Au films (3 nm thick) on Si/SiO_2 [Fig. 1(a)] and TiO_2-based surfaces by solid-state dewetting under thermal treatments > 500 °C (for details see the Experimental Methods). They are characterized by quite irregular shape and size, as well as variable interparticle spacings, due to the general tendency to reshape asymmetrically when increasing the size. Gold islands deviate from the ideal spherical geometries toward disks and rodlike ellipsoids with multiple facets, whose formation mechanism is fully described elsewhere [58–60]. Despite the irregularity in geometrical shapes, the average diameter for spherical particles spans within 15–40 nm (Fig. S2, Supplemental Material [54]), in accordance with data in the literature for similar evaporated Au layer thicknesses [61].

Topography of Au NPs in sandwiches was analyzed by AFM to determine the average NP height before complete embedding (Fig. S3, Supplemental Material [54]). AFM scans reveal rounded NPs with a mean height within 18–22 nm, exhibiting no consistent variations among different substrates, with maximum peaks up to 50 nm. These values are in accordance with average heights measured from cross-section SEM images (13–17 nm). A slight trend can be seen in lateral average dimension of Au particles grown on different surfaces, weakly increasing from bare silicon, to TiO_2 and doped TiO_2, associated with a reduction of the coverage from 28 to 23% [Fig. 1(b)]. This slight discrepancy in geometry is attributed to the different surface process during dewetting, as adhesion and mobility of species change for each metal-substrate couple [62,63]. The particle size distribution is broad ($\sim$7 nm), but the average diameter remains $\sim$25 nm for all substrates. This result is fundamental to minimize any possible contribution from geometrical variability on the LSPR band

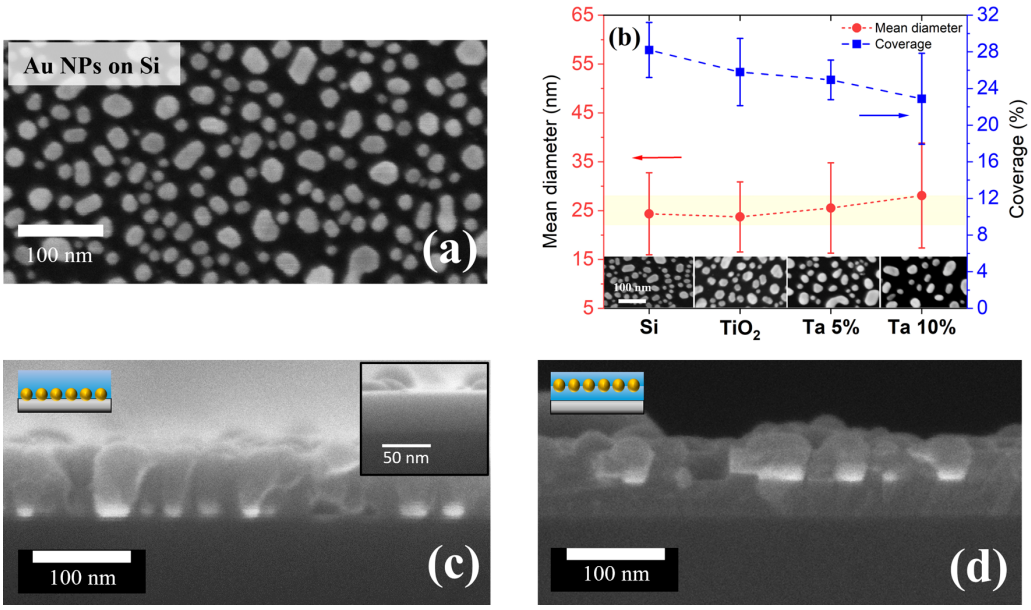

FIG. 1. (a) Scanning electron microscopy (SEM) image (top view) of Au nanoparticles (NPs) deposited on Si. (b) Mean diameter and coverage for different underlayer substrates (with associated SEM images) extracted from statistical distributions. Cross-section SEM images (and schematical representations) of final (c) Au-bottom and (d) Au-sandwich configurations where Au NPs are embedded in Ta(5%):TiO_2. The inset in (c) displays Ta(5%):TiO_2 compact film for reference.

that can build up with the effect of the dielectric surroundings complicating the interpretation of the optical spectra.

The addition of Au NPs by means of a multiple-step procedure affects the morphology and the structure of the TCOs, both in the case of Au NPs at the substrate (Au-bottom) and within the films (Au-sandwich). As clearly visible from the cross-section SEM images of annealed Au-TCO (Ta 5%) composites [Figs. 1(c) and 1(d)], Au NPs act as nucleation sites for the subsequent deposited layer, inducing a directionality in crystallite growth both during deposition and after thermal annealing [63–65]. Compactness is partially lost with respect to Au-free samples [inset in Fig. 1(c)], and the presence of several crystalline domains may degrade the crystallinity, introducing structural defects. As a first qualitative evaluation, the vertical grain size of crystallites is probably limited by the thickness of films, whereas lateral grain size, identified with the width of crystalline domains visible in SEM images, can be approximatively estimated as a few tens of nanometers. No noticeable differences are present in morphology among Au-TiO_2 and Au-TCO nanocomposites; hence, the SEM images are not reported.

In this paper, Raman analysis has been performed with the aim to understand the effect of gold addition on the crystalline quality of TiO_2-based TCO samples. Vibrational properties of Ta-doped TiO_2 have been widely investigated in the past and described elsewhere [42,43,57,66]; effective substitutional doping by Ta leads to a blueshift of the $E_g(1)$ peak of TiO_2 anatase. The Raman spectra of Au-TCO annealed composites compared with their Au-free references are presented in Figs. S4 and S5 in the Supplemental Material [54]. The presence of gold does not prevent an efficient anatase crystallization of the matrix, although incorporation of Au NPs seems to partially degrade the crystallinity of Ta:TiO_2, both in Au-sandwich and Au-bottom composites. For further details, refer to the Supplemental Material [54].

B. Electrical properties

The investigation of electrical performances is important in view of designing a multifunctional system combining transparency, conductivity, and tunable plasmonic properties. However, a complete understanding of electrical behavior in Au-TCO systems is not trivial because a mixture of metals and doped semiconductors involves different conduction mechanisms at once. For this reason, effective properties should be discussed, where different phenomena can take place at the same time, making the identification of the gold contribution to conduction not an elementary task.

Resistivity ρ, as obtained by resistivity measurements, are reported in Fig. 2 as a function of the Au configuration (Au-free samples are shown for reference) in the case of TCO composites of different Ta content (5% and 10% at.). Conducting properties arise because Ta addition activates *n*-type doping. The values corresponding to TiO_2 and Au-TiO_2 films are not reported, as the resistivity was too high to be detected by our experimental setup [43].

The resistivity increases with Au addition in all configurations, as expected from the lower degree of crystallinity previously discussed, along with additional scattering of carriers at the Au-TCO interface. Moreover, the lack of a continuous metal path, the high size dispersion of NPs, as well as the several interfaces and lattice distortions can favor scattering of carriers at the metal-matrix interface, leading to a general degradation of Au-TCO electrical properties [52]. However, resistivity remains low between 1×10^{-3} and $3.6 \times 10^{-3}\ \Omega\,\mathrm{cm}$, the same order of magnitude of Au-free films, proving that transparent TCO films can incorporate Au NPs and still maintain good conducting properties.

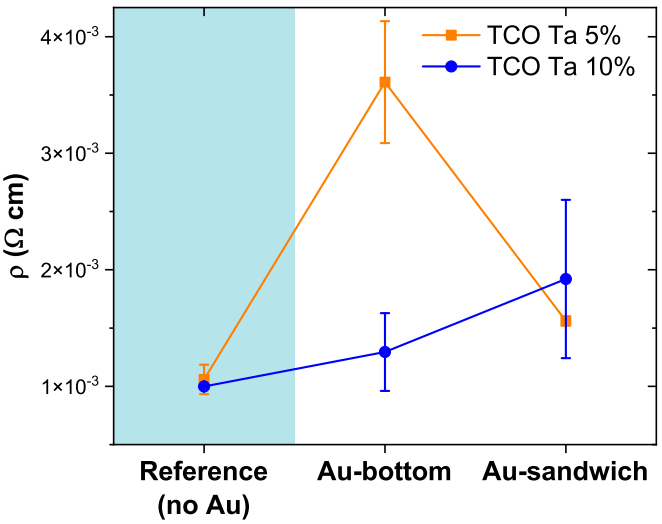

FIG. 2. Resistivity ρ of Au-bottom and Au-sandwich configurations with Ta 5% (orange) and Ta 10% (blue) transparent conductive oxide (TCO) matrix compared with the reference Ta:TiO_2 film of same thickness without gold.

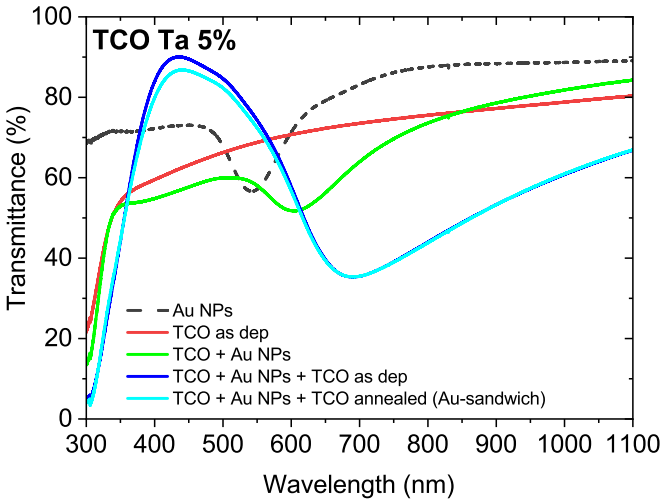

FIG. 3. Direct transmittance spectra measured on each synthesis procedure step for an Au transparent conductive oxide (TCO) Ta 5% sandwich: as deposited (as dep) 35-nm-thick TCO layer (red); 35-nm-thick TCO with Au nanoparticles (NPs) on top after vacuum annealing (green); addition on top of the second 35-nm-thick TCO layer as deposited (blue); final vacuum annealed sandwich (light blue). Transmittance of Au NPs on glass (after air annealing) is shown as reference (black, dashed line).

Some minor fluctuations detected in resistivity among different configurations and with different Ta contents are related to the tradeoff between carrier density and mobility, as further analyzed in Figs. S6(a) and S6(b) in the Supplemental Material [54].

C. Optical properties

1. Experimental transmittance spectra of Au-bottom and Au-sandwich nanocomposites

The optical evolution of direct transmittance measured at each synthesis step of the Au-TCO sandwiches (with Ta 5%) is shown in Fig. 3. The spectrum of Au NPs deposited on glass is shown as a reference for the Au NP plasmonic properties. Pure Ta(5%):TiO_2 film (as deposited, 35 nm thick) is transmitting $> 70\%$ in the visible region, before UV interband absorption occurring at 320 nm. In the next step, Au NPs are formed on top of the TCO, by combining Au evaporation and vacuum annealing. A dip in the transmittance at 610 nm arises due to the excitation of the LSPR of Au NPs. After encapsulating the particles by another 35 nm layer, the LSPR minimum is significantly broadened and redshifted up to 690 nm. The difference before and after embedding is a clear fingerprint of the variation of the effective dielectric environment between the two cases. The additional thermal treatment required to crystallize the second TCO layer does not alter the transmittance curve. This behavior indicates that Au NPs are not subjected to considerable size or shape changes upon annealing, and the LSPR position and width remain unmodified. Hence, thermal-activated diffusion of Au atoms into the solid matrix can be considered marginal [67], and the LSPR band variation is mostly attributed to a change in the surrounding environment, i.e., the degree of integration.

For a better understanding of the optical spectra and thus properly correlating Au plasmon shift and permittivity of the matrix, we anticipate that, for TiO_2-based TCOs, an increase in doping content is associated with a reduction of the real part of the refractive index in the VIS-NIR range [31,68,69], as also proved by spectroscopic ellipsometry analyzed below. As it will be fully described later in the text, in the range where Au LSPR is localized, the main difference in the real component of the electrical permittivity of the matrix (ε_1, extracted at 700 nm) occurs between doped and undoped TiO_2 (6.2), with only slight modifications between TCO Ta 5% (5.46) and TCO Ta 10% (5.33).

Figure 4 provides total transmittance spectra of all Au-bottom and Au-sandwich samples. In Au-bottom configurations [Fig. 4(a)] the Au plasmon excitation is subjected to a consistent redshift with respect to Au NPs exposed to air or glass, whose LSPR is positioned roughly at 550 nm, in agreement with the literature [70]. This behavior is attributed mainly to the sensitivity of the plasmon peak to the dielectric surrounding [1,2,5,11]. However, the transmittance minimum associated with Au LSPR (T_{LSPR}) at the resonant wavelength (λ_{LSPR}) does not significantly shift for a differently doped oxide host [3]. The LSPR minimum moves from 670 nm in TiO_2 to 652 nm in Ta(5%):TiO_2 and 700 nm in Ta(10%):TiO_2.

On the contrary, an evident trend is observed in Au-sandwich composites [Fig. 4(b)], where the resonance λ_{LSPR} blueshifts from 772 nm in TiO_2 to 670 nm in Ta(10%):TiO_2. Notably, the entity of the blueshift is more pronounced in sandwiches than bottoms, along with a broader and more intense plasmonic response (deeper transmittance minimum T_{LSPR}), revealing the role of the embedding geometry. Indeed, a stronger effect of the dielectric function is expected in the sandwich because Au NPs are completely embedded in the TCO host and experience the largest variation in dielectric environment. It should be noted that, although NP size, shape, or interparticle distance can affect the plasmon resonance [5], such contributions are secondary compared with the

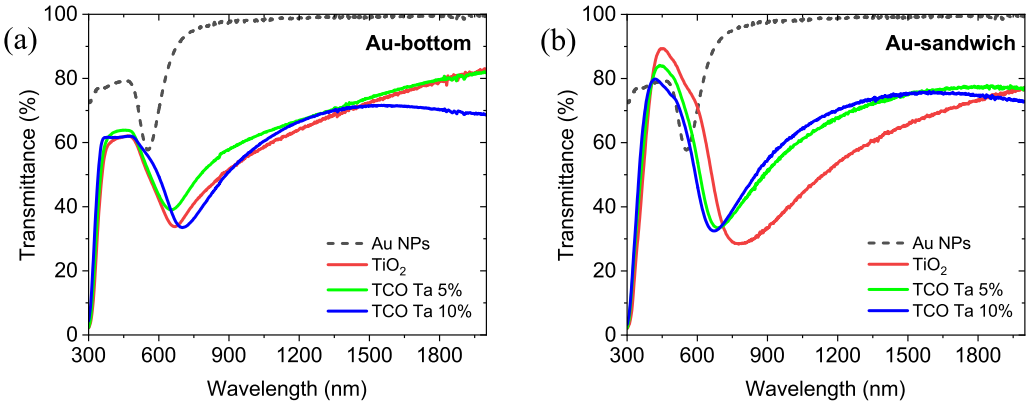

FIG. 4. Total transmittance spectra of (a) Au-bottom and (b) Au-sandwich configurations as a function of different Ta doping (5%, 10%, and bare TiO_2). Transmittance of Au NPs on glass substrate are shown for reference (black, dashed line).

dielectric function of the matrix because geometrical fluctuations detected among samples are weak [Fig. 1(b)]. Furthermore, additional effects can contribute, inherent in reflections or scattering; thus, transmission analyses are not sufficient to discard other possible phenomena. Interference fringes arising from multiple reflection at ambient-film and film-substrate interfaces [71] can overlap T_{LSPR}, hindering a correct estimation of the LSPR position and width. These issues are partially addressed in the next paragraph, where the modeling of effective dielectric functions allows the disentanglement of the contribution of Au plasmon LSPR.

2. *Effective modeling of Au-NP layer in bottom and sandwich configuration*

In this subsection, we try to verify the correlation between LSPR shift and dielectric function of the matrix by modeling total transmittance spectra in Figs. 4(a) and 4(b) to obtain the real and imaginary part of the effective dielectric functions ε_1 and ε_2 of the Au-NP layer. This approach enables the direct investigation of the plasmonic behavior of embedded Au NPs.

For the modeling of the experimental data of Figs. 4(a) and 4(b), the system was considered as a stack of dielectric layers, each characterized by its thickness and complex dielectric function, representing the various physical layers of the samples, with Fresnel boundary conditions. The calculated transmittance spectra were compared with the experimental ones, and the dielectric or morphological characteristics of the layers were adjusted to achieve the best fit. Bottom to top, the model for the Au-bottom samples [Fig. 4(a)] included (i) a transparent glass substrate, (ii) an effective layer representative of the Au NPs deposited on the glass substrate, and (iii) the 70-nm-thick (Ta-doped) TiO_2 film. For the Au-sandwich samples [Fig. 4(b)], the model was (i) a transparent glass substrate, (ii) the 35-nm-thick (Ta-doped) TiO_2 film, (iii) an effective layer representative of the Au NPs deposited on the Ta:TiO_2 surface, and (iv) one more 35-nm-thick layer of (Ta-doped) TiO_2 film of the same doping.

In the model, we used the dielectric functions of TiO_2, Ta(5%):TiO_2, and Ta(10%):TiO_2 already reported in Ref. [66] and here only slightly adapted to fulfill the optimal fitting of transmittance curves [Figs. 4(a) and 4(b)]. The Au-NP layer was modeled using Kramers-Kronig-consistent PSEMI oscillators, i.e., parameterized functions widely employed for modeling the optical response of crystalline semiconductors [55,56]. The thickness of the effective Au layer is an effective parameter, whose only constraint is to be of the same order of magnitude of the mean Au-NP dimension. Here, we are not interested in discussing the thickness of this effective layer nor the numerical magnitude of the effective dielectric constant, while we focus on the wavelength of the resonance. A thickness of 9 nm for each system was found to provide a good fit to the experimental transmittance.

Figure S7, shown in the Supplemental Material [54], compares experimental transmission data to the fitted values. The good matching proves the reliability of the resulting optical outputs presented in Fig. 5. The dielectric constants of the TiO_2-based films [Fig. 5(a)] are in good agreement with trends reported in the literature for TiO_2 anatase, with 3.2 eV bandgap [30,68,69,72–74]. The magnification at 250–350 nm in the inset of Fig. 5(a) clearly shows that higher Ta concentration causes a blueshift of the absorption band, associated with an increase in the optical bandgap according to Moss-Burstein relation [68,69,75]. When comparing doped and undoped TiO_2, ε_1 is lower for films with higher Ta doping content ($\lambda > 500$ nm), hence revealing the influence of free charge carriers arising from Ta substitutional dopants on the dielectric function [30,76,77]. In the visible region, all TiO_2-based films are highly transparent materials; hence, absorption is very low. At longer wavelength, ε_2 rises with higher doping content because Drude-like free carrier absorption increases with larger carrier densities [42,43,57,78].

The effective dielectric functions ε_1 and ε_2 of the Au layer, yielding the best agreement with the experimental transmittance, are displayed in Figs. 5(b) and 5(c) (bottom and sandwich configurations, respectively). Effective optical constants of Au NPs on glass (black, dashed lines) are shown for reference. In the visible region, the effective ε of Au NPs on glass exhibit a strong resonance, which is identified as the Au LSPR. Hence, the real component (ε_1) is characterized by a wiggled line shape centered ∼550 nm, corresponding to the LSPR, while in ε_2, an absorption peak at 550 nm is observed. The resonance position agrees with previous estimations from

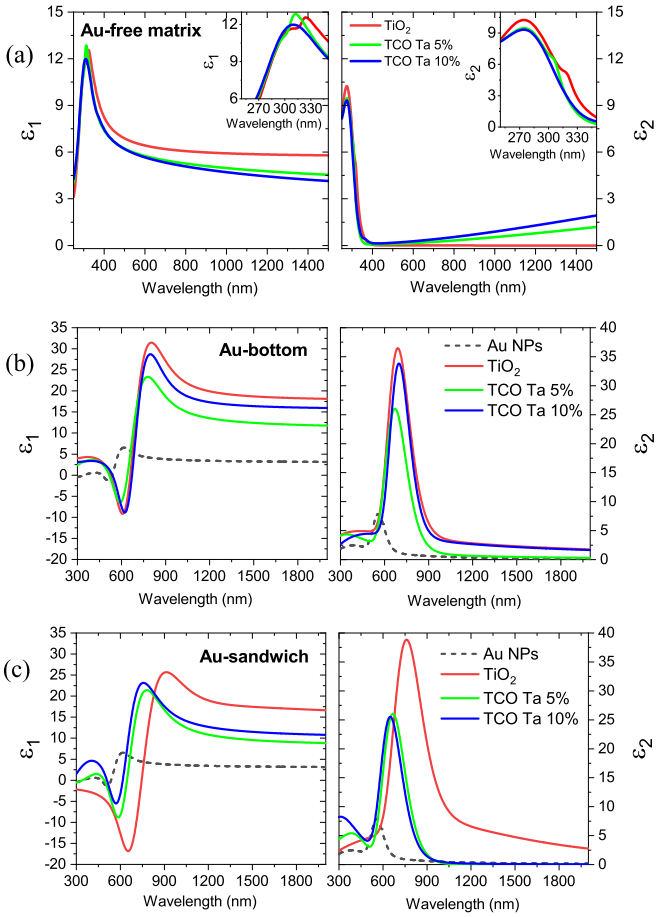

FIG. 5. (a) Real (left, ε_1) and imaginary (right, ε_2) components of the dielectric functions of Au-free TiO_2, transparent conductive oxide (TCO; 5%, 10% Ta) thin films extracted from ellipsometry. The insets show the expanded view of curves within 250–350 nm (ε_1 and ε_2). (b) Real (left, ε_1) and imaginary (right, ε_2) components of the effective dielectric functions of Au-NP layer modeled in a bottom configuration with TiO_2, TCOs (5%, 10% Ta) obtained by total transmittance fitting. (c) Real (left, ε_1) and imaginary (right, ε_2) components of the effective dielectric functions of Au NP layer modeled in a sandwich configuration with TiO_2, TCOs (5%, 10% Ta) obtained by transmittance fitting. Effective optical constants of Au NPs deposited on glass are shown for reference (black, dashed line).

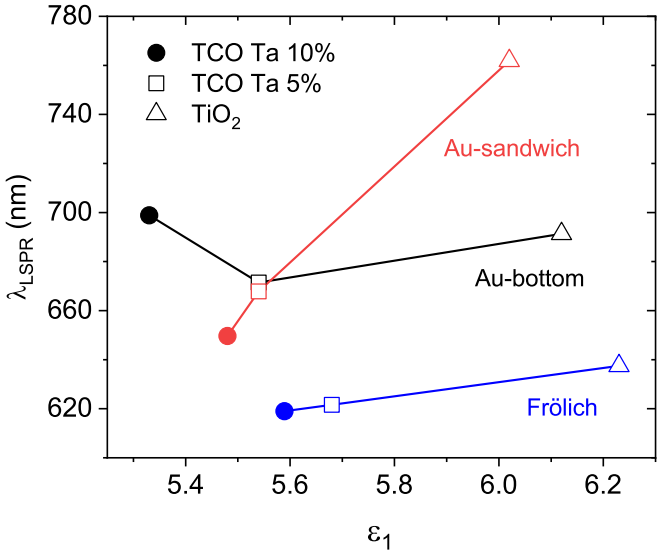

FIG. 6. Plasmon resonance of Au nanoparticles (NPs; λ_{LSPR}) taken from ε_2 in Figs. 5(b) and 5(c) as a function of the ε_1 of the surrounding medium [transparent conductive oxide (TCO) Ta 10%, TCO Ta 5%, TiO_2, extracted at the localized surface plasmon resonance (LSPR) wavelength] embedded in two configurations (Au-bottom, black curve, and Au-sandwich, red curve) compared with the expected dependence based on the Frölich condition (blue curve).

transmittance spectra (550 nm) (Fig. (4)) and with data available in the literature [79,80].

In the Au-bottom configuration, Fig. 5(b), the corresponding effective dielectric function of the Au NP layer is strongly modified with respect to the glass reference. The LSPR redshifts more than 150 nm in all films compared with Au NPs on glass and increases in magnitude [25,81]. However, no clear trend of the LSPR characteristics was observed as a function of doping, highlighting the weak effect of the TiO_2 matrix when inserted in the systems only as an overlayer.

In the Au-sandwich configuration, Fig. 5(c), the effective permittivity shows a marked change with respect to the reference Au-glass case. Here, the blueshift of the Au NP resonance is now noticeable when increasing matrix doping. The absorption peak at λ_{LSPR} blueshifts clearly from 760 nm (TiO_2) to 667 and 650 nm in Ta-doped TiO_2 (5%, 10% at. Ta). This behavior results from the lower permittivity of the surrounding matrix properly modulated through doping (i.e., higher carrier density). It should be noted that all Au LSPR peaks in ε_2 are in excellent agreement with absorbance spectra of the films, in which the contribution of experimental reflectance has been also considered (Fig. S8, Supplemental Material [54]), hence further confirming the physical reliability of the optical model.

The local-environment dependence of the LSPR is an established effect [82]. However, if we compare the expected dependence (based on the Frölich condition) of the LSPR wavelength versus the dielectric permittivity of the matrix (Fig. 6, blue symbols) with the experimental data (Fig. 6, black and red symbols for the bottom and sandwich configuration, respectively), we notice that significant differences arise. Leaving the bottom configuration aside (the environment is inhomogeneous in this case), we observe that the LSPR in the sandwich case is strongly redshifted with respect to the simple theoretical expectations and that the LSPR dependence on the permittivity is much stronger. The general redshift is easily interpreted as a result of the mutual NP electromagnetic interaction [7], whereas we suggest that the strong variation of the LSPR wavelength in the $5.5 < \varepsilon_1 < 6$ range is related to the peculiar characteristics of the embedding medium that, while preserving the LSPR, is nonetheless an electrical conductor [83].

We therefore suggest that the Au LSPR could include the contribution of some charge transfer mechanisms activated at the gold-matrix interfaces [21–23,51,52,84–86]. Previous works demonstrated that charging of the particle surface can lead to small shifts in LSPR positions, depending on several

factors (e.g., surface-to-volume ratio, size of NPs) [84,87]. For the systems investigated here, we do not attempt to disentangle the possible entity of the shift related to charge transfer, although the remarkable difference observed between the experimental trends and the simple Frölich-condition calculation may be exploited to this end.

IV. CONCLUSIONS

In summary, nanocomposites made of Au NPs and Ta:TiO_2 TCO films were synthetized through a multistep method of preparation, combining PLD, Au evaporation, and ad hoc thermal treatments. The localized plasmon resonance and thus the optical response of Au NPs was successfully controlled by operating directly on the dielectric properties of the surroundings through the configuration of NP integration. The configuration was demonstrated to play an important role on resonance position and intensity; fully embedded Au NPs in a sandwich setup experienced the largest modulation of LSPR, with a considerable redshift (550–760 nm) and broadening compared with air-exposed NPs. In the case of Au NPs positioned between the substrate and the TCO (i.e., bottom configuration), the effect is less intense (550–700 nm), but the same trend (redshift) is reproduced. Another approach consisted of varying the doping level of the TCO to induce a change in the electrical permittivity of the matrix by means of the Ta content in the TCO. An increasing degree of doping in the TiO_2-based hosts (Ta 0, 5, 10% at.) proved to blueshift efficiently Au plasmon position, for sandwich configuration, in a wide wavelength range between 650 and 760 nm, going beyond the tunability predicted by simple theoretical models (e.g., Frolich resonance condition).

Despite the large LSPR modulation, structural and electrical characteristics of Au-TCO nanocomposites were degraded upon the addition of Au NPs with irregular geometries. We showed that Au NPs behave as nucleation centers for the growth of TCO crystallites, acting as scattering centers and introducing structural disorder. However, the lowest resistivity reached is $\sim 1.5 \times 10^{-3}\,\Omega\,\mathrm{cm}$ in Au-Ta(10%):TiO_2 architectures, proving that Au NPs can be incorporated in TCO films while maintaining good electrical conduction, comparable with Au-free TCO films. At the same time, a different fabrication procedure, i.e., multistep depositions of Au NPs and matrix in the same PLD process, may improve the structural quality and electrical properties. More investigations are required to get a full comprehension of these complex nanosystems, by identifying the contribution of size or shape of NPs or charge transfer mechanisms on the LSPR redshift, mainly dictated by the dielectric function of the TCO.

Concluding, metal-TCO conductive nanocomposite films have been subjected to a full material characterization that can potentially offer a platform for designing original and multifunctional optoelectronic devices. The plasmonic character owned by TCOs can possibly widen the wavelength of operation of such nanostructures from the visible up to the infrared. Additionally, these devices are eligible candidates for active plasmonic modulation, in which carriers can be injected by applying an electric bias (field effect). Moreover, the tunability of plasmon resonance achieved in Au-TCO architectures paves the way toward the development of optical-plasmonic metamaterials, such as multilayers of sandwiches, able to engineer plasmonic features in multifunctional transparent electrodes (e.g., for photovoltaics).

ACKNOWLEDGMENTS

This project has received financial support from the European Union's Horizon 2020 research and innovation programme under the Marie Skłodowska-Curie Grant Agreement No. 799126.

[1] V. Amendola, R. Pilot, M. Frasconi, O. M. Maragò, and M. A. Iatì, Surface plasmon resonance in gold nanoparticles: A review, J. Phys: Condens. Matter **29**, 203002 (2017).

[2] M. A. Garcia, Surface plasmons in metallic nanoparticles: fundamentals and applications, J. Phys. D: Appl. Phys. **44**, 283001 (2011).

[3] S. A. Maier, *Plasmonics: Fundamentals and Applications* (Springer US, New York, 2007), p. 65.

[4] L. M. Liz-Marzán, Tailoring surface plasmons through the morphology and assembly of metal nanoparticles, Langmuir **22**, 32 (2005).

[5] K. L. Kelly, E. Coronado, L. L. Zhao, and G. C. Schatz, The optical properties of metal nanoparticles: the influence of size, shape, and dielectric environment, J. Phys. Chem. B **107**, 668 (2003).

[6] S. Kumar Ghosh, and T. Pal, Interparticle coupling effect on the surface plasmon resonance of gold nanoparticles: from theory to applications, Chem. Rev. **107**, 4797 (2007).

[7] P. K. Jain, and M. A. El-Sayed, Plasmonic coupling in noble metal nanostructures, Chem. Phys. Lett. **487**, 153 (2010).

[8] K. S. Lee, and M. A. El-Sayed, Gold and silver nanoparticles in sensing and imaging: sensitivity of plasmon response to size, shape, and metal composition, J. Phys. Chem. B **110**, 19220 (2006).

[9] R. Proietti Zaccaria, F. Bisio, G. Das, G. Maidecchi, M. Caminale, C. D. Vu, F. De Angelis, E. Di Fabrizio, A. Toma, and M. Canepa, Plasmonic color-graded nanosystems with achromatic subwavelength architectures for light filtering and advanced SERS detection, ACS Appl. Mater. Interfaces **8**, 8024 (2016).

[10] E. Petryayeva, and U. J. Krull, Localized surface plasmon resonance: nanostructures, bioassays and biosensing—a review, Anal. Chim. Acta. **706**, 8 (2011).

[11] M. M. Miller, and A. A. Lazarides, Sensitivity of metal nanoparticle surface plasmon resonance to the dielectric environment, J. Phys. Chem. B **109**, 21556 (2005).

[12] H. Chen, X. Kou, Z. Yang, W. Ni, and J. Wang, Shape- and size-dependent refractive index sensitivity of gold nanoparticles, Langmuir **24**, 5233 (2008).

[13] H. A. Atwater, and A. Polman, Plasmonics for improved photovoltaic devices, Nat. Mater. **9**, 205 (2010).

[14] C. Clavero, Plasmon-induced hot-electron generation at nanoparticle/metal-oxide interfaces for photovoltaic and photocatalytic devices, Nat. Photonics **8**, 95 (2014).
[15] S. C. Warren, and E. Thimsen, Plasmonic solar water splitting, Energy Environ. Sci. **5**, 5133 (2012).
[16] S. Linic, P. Christopher, and D. B. Ingram, Plasmonic-metal nanostructures for efficient conversion of solar to chemical energy, Nat. Mater. **10**, 911 (2011).
[17] P. K. Jain, X. Huang, I. H. El-Sayed, and M. A. El-Sayed, Review of some interesting surface plasmon resonance-enhanced properties of noble metal nanoparticles and their applications to biosystems, Plasmonics **2**, 107 (2007).
[18] M. E. Stewart, C. R. Anderton, L. B. Thompson, J. Maria, S. K. Gray, J. A. Rogers, and R. G. Nuzzo, Nanostructured plasmonic sensors, Chem. Rev. **108**, 494 (2008).
[19] Z. Wang, C. Chen, K. Wu, H. Chong, and H. Ye, Transparent conductive oxides and their applications in near infrared plasmonics, Phys. Status Solidi A **216**, 1700794 (2019).
[20] G. V. Naik, V. M. Shalaev, and A. Boltasseva, Alternative plasmonic materials: beyond gold and silver, Adv. Mater. **25**, 3264 (2013).
[21] P. Sen, D. Kar, R. Laha, M. Balasubrahmaniyam, and S. Kasiviswanathan, Hot electron mediated enhancement in the decay rates of persistent photocurrent in gold nanoparticles embedded indium oxide films, Appl. Phys. Lett. **114**, 211103 (2019).
[22] N. Gogurla, R. K. Chowdhury, S. Battacharya, P. K. Datta, and S. K. Ray, Plasmon charge transfer dynamics in layered Au-ZnO nanocomposites, J. Appl. Phys. **127**, 053105 (2020).
[23] J. S. Pelli Cresi, M. C. Spadaro, S. D'Addato, S. Valeri, S. Benedetti, A. Di Bona, D. Catone, L. Di Mario, P. O'Keeffe, A. Paladini, G. Bertoni, and P. Luches, Highly efficient plasmon-mediated electron injection into cerium oxide from embedded silver nanoparticles, Nanoscale **11**, 10282 (2019).
[24] B. R. Bricchi, M. Ghidelli, L. Mascaretti, A. Zapelli, V. Russo, C. S. Casari, G. Terraneo, I. Alessandri, C. Ducati, and A. Li Bassi, Integration of plasmonic au nanoparticles in TiO_2 hierarchical structures in a single-step pulsed laser co-deposition, Mater. Des. **156**, 311 (2018).
[25] J. Borges, R. M. S. Pereira, M. S. Rodrigues, T. Kubart, S. Kumar, K. Leifer, A. Cavaleiro, T. Polcar, M. I. Vasilevskiy, and F. Vaz, Broadband optical absorption caused by the plasmonic response of coalesced Au nanoparticles embedded in a TiO_2 matrix, J. Phys. Chem. C **120**, 16931 (2016).
[26] D. Costa, J. Oliveira, M. S. Rodrigues, J. Borges, C. Moura, P. Sampaio, and F. Vaz, Development of biocompatible plasmonic thin films composed of noble metal nanoparticles embedded in a dielectric matrix to enhance Raman signals, Appl. Surf. Sci. **496**, 143701 (2019).
[27] J. Borges, M. S. Rodrigues, C. Lopes, D. Costa, F. M. Couto, T. Kubart, B. Martins, N. Duarte, J. P. Dias, A. Cavaleiro, T. Polcar, F. Macedo, and F. Vaz, Thin films composed of Ag nanoclusters dispersed in TiO_2: influence of composition and thermal annealing on the microstructure and physical responses, Appl. Surf. Sci. **358**, 595 (2015).
[28] D. S. Ginley, *Handbook of Transparent Conductors* (Springer US, Boston, 2011).
[29] M. R. Ananthan, P. Malar, T. Osipowicz, S. Varma, and S. Kasiviswanathan, Growth and characterization of Au nanoparticles embedded in In_2O_3 composite films, Thin Solid Films **622**, 78 (2017).
[30] C. M. Maghanga, G. A. Niklasson, and C. G. Granqvist, Optical properties of sputter deposited transparent and conducting TiO_2:Nb films, Thin Solid Films **518**, 1254 (2009).
[31] A. V. Manole, M. Dobromir, M. Gîrtan, R. Mallet, G. Rusu, and D. Luca, Optical properties of Nb-doped TiO_2 thin films prepared by sol-gel method, Ceram. Int. **39**, 4771 (2013).
[32] C. G. Granqvist, Transparent conductors as solar energy materials: a panoramic review, Sol. Energy Mater. Sol. Cells **91**, 1529 (2007).
[33] S. Sarker, H. W. Seo, Y. K. Jin, M. A. Aziz, and D. M. Kim, Transparent conducting oxides and their performance as substrates for counter electrodes of dye-sensitized solar cells, Mater. Sci. Semicond. Process. **93**, 28 (2019).
[34] N. M. Le, J. C. Park, J. Kim, and B. T. Lee, Realization of highly conductive and transparent GaZnO/InCdO/GaZnO films for the enhancement of solar cell efficiency, Sol. Energy Mater. Sol. Cells **198**, 1 (2019).
[35] S. Ghosh, M. Saha, S. Paul, and S. K. De, Shape controlled plasmonic Sn doped CdO colloidal nanocrystals: a synthetic route to maximize the figure of merit of transparent conducting oxide, Small **13**, 1602469 (2017).
[36] M. Morales-Masis, F. Dauzou, Q. Jeangros, A. Dabirian, H. Lifka, R. Gierth, M. Ruske, D. Moet, A. Hessler-Wyser, and C. Ballif, An indium-free anode for large-area flexible OLEDs: defect-free transparent conductive zinc tin oxide, Adv. Funct. Mater. **26**, 384 (2016).
[37] D. U. Yildirim, A. Ghobadi, M. C. Soydan, O. Atesal, A. Toprak, M. D. Caliskan, and E. Ozbay, Disordered and densely packed ITO nanorods as an excellent lithography-free optical solar reflector metasurface, ACS Photonics **6**, 1812 (2019).
[38] T. Hitosugi, N. Yamada, S. Nakao, Y. Hirose, and T. Hasegawa, Properties of TiO_2-based transparent conducting oxides, Phys. Status Solidi A **207**, 1529 (2010).
[39] Y. Furubayashi, T. Hitosugi, Y. Yamamoto, K. Inaba, G. Kinoda, Y. Hirose, T. Shimada, and T. Hasegawa, A transparent metal: Nb-doped anatase TiO_2, Appl. Phys. Lett. **86**, 252101 (2005).
[40] Y. Liu, Y. D. Qiao, and G. Yang, Effect of thickness on the structural, morphological, electrical and optical properties of Nb plus Ta co-doped TiO_2 films deposited by RF sputtering, Appl. Phys. A **124**, 530 (2018).
[41] X. Lü, X. Mou, J. Wu, D. Zhang, L. Zhang, F. Huang, F. Xu, and S. Huang, Improved-performance dye-sensitized solar cells using Nb-doped TiO_2 electrodes: efficient electron injection and transfer, Adv. Funct. Mater. **20**, 509 (2010).
[42] P. Mazzolini, T. Acartürk, D. Chrastina, U. Starke, C. S. Casari, G. Gregori, and A. Li Bassi, Controlling the electrical properties of undoped and Ta-doped TiO_2 polycrystalline films via ultrafast-annealing treatments, Adv. Electron. Mater. **2**, 1500316 (2016).
[43] P. Mazzolini, P. Gondoni, V. Russo, D. Chrastina, C. S. Casari, and A. Li Bassi, Tuning of electrical and optical properties of highly conducting and transparent Ta doped TiO_2 polycrystalline films, J. Phys. Chem. C **119**, 6988 (2015).
[44] S. Chuang, C. Tsung, C. Chen, S. Ou, R. Horng, C. Lin, and D. Wuu, Transparent conductive oxide films embedded with plasmonic nanostructure for light-emitting diode applications, ACS Appl. Mater. Interfaces **7**, 2546 (2015).

[45] C. Guillén, and J. Herrero, TCO/metal/TCO structures for energy and flexible electronics, Thin Solid Films **520**, 1 (2011).

[46] K. Fleischer, E. Arca, and I. V. Shvets, Improving solar cell efficiency with optically optimised TCO layers, Sol. Energy Mater. Sol. Cells **101**, 262 (2012).

[47] H. Ferhati, F. Djeffal, and A. Benhaya, Optimized high-performance ITO/Ag/ITO multilayer transparent electrode deposited by RF magnetron sputtering, Superlattices and Microstruct. **129**, 176 (2019).

[48] M. Huang, Z. Hameiri, H. Gong, W. Wong, A. G. Aberle, and T. Mueller, Hybrid silver nanoparticle and transparent conductive oxide structure for silicon solar cell applications, Phys. Status Solidi RRL **8**, 399 (2014).

[49] F. Wang, Q. Wang, G. Xu, R. Hui, and J. Wu, Light trapping on plasmonic-photonic nanostructured fluorine-doped tin oxide, J. Phys. Chem. C **117**, 11725 (2013).

[50] C. K. T. Chew, C. Salcianu, P. Bishop, C. J. Carmalt, and I. P. Parkin, Functional thin film coatings incorporating gold nanoparticles in a transparent conducting fluorine doped tin oxide matrix, J. Mater. Chem. C **3**, 1118 (2015).

[51] P. Huang, F. Qin, and J. Lee, Role of the interface between ag and ZnO in the electric conductivity of Ag nanoparticle-embedded ZnO, ACS Appl. Mater. Interfaces **12**, 4715 (2020).

[52] P. Huang, F. Qin, Z. Xiong, H. Shim, T. Gao, P. Leu, and J. Lee, Novel carrier doping mechanism for transparent conductor: electron donation from embedded ag nanoparticles to the oxide matrix, ACS Appl. Mater. Interfaces **9**, 19973 (2017).

[53] C. Ho, D. Yeh, V. Su, C. Yang, P. Yang, M. Pu, C. Kuan, I. Cheng, and S. Lee, Plasmonic multilayer nanoparticles enhanced photocurrent in thin film hydrogenated amorphous silicon solar cells, J. Appl. Phys. **112**, 23113 (2012).

[54] See Supplemental Material at http://link.aps.org/supplemental/10.1103/PhysRevMaterials.6.025201 for details about the synthesis process for Au-TCO nanocomposites, statistical distributions of Au NP diameters, AFM image of Au NPs used in nanocomposites, Raman spectra of Au-sandwich and Au-bottom configuration, electrical properties, experimental transmission spectra with fitted values extracted from ellipsometry on similar films, and logarithmic absorbance of Au nanocomposites.

[55] C. Herzinger and B. Johs, *Guide to Using WVASE32* (J. A. Woollam Co., Lincoln, NE, 1996).

[56] C. M. Herzinger and B. D. Johs, Dielectric function parametric model, and method of use, U.S. Patent No. 5,796,983. Washington DC: U.S. Patent and Trademark Office (assigned to J. A. Woollam Co. Inc., 1998).

[57] P. Mazzolini, V. Russo, C. S. Casari, T. Hitosugi, S. Nakao, T. Hasegawa, and A. Li Bassi, Vibrational-electrical properties relationship in donor-doped TiO_2 by Raman spectroscopy, J. Phys. Chem. C **120**, 18878 (2016).

[58] C. V. Thompson, Solid-state dewetting of thin films, Annu. Rev. Mater. Res. **42**, 399 (2012).

[59] F. Leroy, Ł. Borowik, F. Cheynis, Y. Almadori, S. Curiotto, M. Trautmann, J. C. Barbé, and P. Müller, How to control solid state dewetting: a short review, Surf. Sci. Rep. **71**, 391 (2016).

[60] T. Karakouz, D. Holder, M. Goomanovsky, A. Vaskevich, and I. Rubinstein, Morphology and refractive index sensitivity of gold island films, Chem. Mater. **21**, 5875 (2009).

[61] D. Gaspar, A. C. Pimentel, T. Mateus, J. P. Leitão, J. Soares, B. P. Falcão, A. Araújo, A. Vicente, S. A. Filonovich, H. Águas, R. Martins, and I. Ferreira, Influence of the layer thickness in plasmonic gold nanoparticles produced by thermal evaporation, Sci. Rep. **3**, 1469 (2013).

[62] P. D. Nsimama, A. Herz, D. Wang, and P. Schaaf, Influence of the substrate on the morphological evolution of gold thin films during solid-state dewetting, Appl. Surf. Sci. **388**, 475 (2016).

[63] A. Tamm, I. O. Acik, T. Arroval, A. Kasikov, H. Seemen, M. Marandi, M. Krunks, A. Mere, K. Kukli, and J. Aarik, Plasmon resonance effect caused by gold nanoparticles formed on titanium oxide films, Thin Solid Films **616**, 449 (2016).

[64] R. Reshmi Krishnan, V. S. Kavitha, M. C. Santhosh Kumar, K. G. Gopchandran, and V. P. Mahadevan Pillai, Properties of Au incorporated In_2O_3 films, Mater. Sci. Semicond. Process. **93**, 134 (2019).

[65] M. Ghidelli, L. Mascaretti, B. R. Bricchi, A. Brognara, T. A. Afifi, V. Russo, C. S. Casari, and A. Li Bassi, Light management in TiO_2 thin films integrated with au plasmonic nanoparticles, Semicond. Sci. Technol. **35**, 035016 (2020).

[66] B. R. Bricchi, M. Sygletou, L. Ornago, G. Terraneo, F. Bisio, C. Mancarella, L. Stasi, F. Rusconi, E. Mogni, M. Ghidelli, P. Biagioni, and A. Li Bassi, Optical and electronic properties of transparent conducting Ta:TiO_2 thin and ultra-thin films: effect of doping and thickness, Mater. Adv. **2**, 7064 (2021).

[67] D. Buso, J. Pacifico, A. Martucci, and P. Mulvaney, Gold-nanoparticle-doped TiO_2 semiconductor thin films: optical characterization, Adv. Funct. Mater. **17**, 347 (2007).

[68] E. Nurfani, R. Kurniawan, S. Muhammady, R. Marlina, I. M. Sutjahja, T. Winata, A. Rusydi, and Y. Darma, Effect of Ta concentration on the refractive index of TiO_2:Ta studied by spectroscopic ellipsometry, AIP Conf. Proc. **1725**, 020057 (2016).

[69] E. Nurfani, I. M. Sutjahja, T. Winata, A. Rusydi, and Y. Darma, Optical properties analysis of Ta-doped TiO_2 thin films on $LaAlO_3$ substrates, AIP Conf. Proc. **1677**, 070008 (2015).

[70] G. Gupta, D. Tanaka, Y. Ito, D. Shibata, M. Shimojo, K. Furuya, K. Mitsui, and K. Kajikawa, Absorption spectroscopy of gold nanoisland films: optical and structural characterization, Nanotechnology **20**, 025703 (2008).

[71] H. Bakkali, E. Blanco, M. Domínguez, and J. S. Garitaonandia, Fabrication and optical properties of nanostructured plasmonic Al_2O_3/Au-Al_2O_3/Al_2O_3 metamaterials, Nanotechnology **28**, 335704 (2017).

[72] G. E. Jellison, L. A. Boatner, J. D. Budai, B. -S. Jeong, and D. P. Norton, Spectroscopic ellipsometry of thin film and bulk anatase (TiO_2), J. Appl. Phys. **93**, 9537 (2003).

[73] H. Tang, K. Prasad, R. Sanjinès, P. E. Schmid, and F. Lévy, Electrical and optical properties of TiO_2 anatase thin films, J. Appl. Phys. **75**, 2042 (1994).

[74] Y. R. Park, and K. J. Kim, Structural and optical properties of rutile and anatase TiO_2 thin films: effects of Co doping, Thin Solid Films **484**, 34 (2005).

[75] W. Zhao, L. He, X. Feng, C. Luan, and J. Ma, Structural, electrical and optical properties of epitaxial Ta-doped titania films by MOCVD, CrystEngComm **20**, 5395 (2018).

[76] A. Kompa, U C., D. Kekuda, and M. Rao K, Investigation on structural, optical and electrical properties of Nb doped titania

films and application of optical model, Mater. Sci. Semicond. Process. **121**, 105293 (2021).

[77] S. Muhammady, E. Nurfani, R. Kurniawan, I. M. Sutjahja, T. Winata, and Y. Darma, The effect of Ta dopant on the electronic and optical properties of anatase TiO_2: a first-principles study, Mater. Res. Express **4**, 024002 (2017).

[78] A. Agrawal, R. W. Johns, and D. J. Milliron, Control of localized surface plasmon resonances in metal oxide nanocrystals, Annu. Rev. Mater. Res. **47**, 1 (2017).

[79] N. M. Figueiredo, and A. Cavaleiro, Dielectric properties of shape-distributed ellipsoidal particle systems, Plasmonics **15**, 379 (2020).

[80] S. N. Wani, A. S. Sangani, and R. Sureshkumar, Effective permittivity of dense random particulate plasmonic composites, J. Opt Soc. Am. B: Opt. Phys. **29**, 1443 (2012).

[81] F. Javed, S. Javed, M. Mujahid, F. U. Inam, and A. S. Bhatti, Modified optical characteristics of TiO_2/Au/TiO_2 thin composite films, Ceram. Int. **45**, 22336 (1981).

[82] L. Novotny, and B. Hecht, *Principles of Nano-Optics* (Cambridge University Press, Cambridge, 2012).

[83] M. Sygletou, S. Benedetti, M. Ferrera, G. M . Pierantozzi, R. Cucini, G. Della Valle, P. Carrara, A. De Vita, A. di Bona, P. Torelli, D. Catone, G. Panaccione, M. Canepa, and F. Bisio, Quantitative ultrafast electron-temperature dynamics in photo-excited Au nanoparticles, Small **17**, 2100050 (2021).

[84] J. S. Pelli Cresi, E. Silvagni, G. Bertoni, M. C. Spadaro, S. Benedetti, S. Valeri, S. D'Addato, and P. Luches, Optical and electronic properties of silver nanoparticles embedded in cerium oxide, J. Chem. Phys. **152**, 114704 (2020).

[85] P. S. Huang, D. H. Kim, and J. K. Lee, Electron emission of Au nanoparticles embedded in ZnO for highly conductive oxide, Appl. Phys. Lett. **104**, 142102 (2014).

[86] M. Sygletou, S. Benedetti, A. di Bona, M. Canepa and F. Bisio, Doping-dependent optical response of a hybrid transparent conductive, oxide/plasmonic medium, J. Phys. Chem. C **126**, 1881 (2022).

[87] M. Moskovits, I. Srnová-Šloufová, and B. Vlčková, Bimetallic Ag-Au nanoparticles: extracting meaningful optical constants from the surface-plasmon extinction spectrum, J. Chem. Phys. **116**, 10435 (2002).